

PSFC/JA-10-29

## Charged-Particle Probing of X-Ray-Driven Inertial-Fusion Implosions

C. K. Li<sup>1</sup>, F. H. Séguin<sup>1</sup>, J. A. Frenje<sup>1</sup>, M. Rosenberg<sup>1</sup>, R. D. Petrasso<sup>1</sup>, P. A. Amendt<sup>2</sup>, J. A. Koch<sup>2</sup>, O. L. Landen<sup>2</sup>, H. S. Park<sup>2</sup>, H. F. Robey<sup>2</sup>, R. P. J. Town<sup>2</sup>, A. Casner<sup>3</sup>, F. Philippe<sup>3</sup>, R. Betti<sup>4</sup>, J. P. Knauer<sup>4</sup>, D. D. Meyerhofer<sup>4</sup>, T. A. Back<sup>5</sup>, J. D. Kilkenny<sup>5</sup>,  
A. Nikroo<sup>5</sup>

<sup>1</sup>Plasma Science and Fusion Center, Massachusetts Institute of Technology, Cambridge, MA 02139, USA.

<sup>2</sup>Lawrence Livermore National Laboratory, Livermore, CA 94550, USA.

<sup>3</sup>CEA/DIF, Arpajon Cedex, France.

<sup>4</sup>Laboratory for Laser Energetics, University of Rochester, Rochester, NY 14623, USA.

<sup>5</sup>General Atomics, San Diego, CA 92186, USA

15 March 2010

Plasma Science and Fusion Center  
Massachusetts Institute of Technology  
Cambridge, MA 02139 USA

The work was performed at the LLE National Laser User's Facility (NLUF), and was supported in part by US DOE (DE-FG52-07NA28059 and DE-FG52-06N826203), LLNL (B543881 and LDRD-ER 898988), and LLE (414090-G), The Fusion Science Center at University of Rochester (412761-G).

Accepted for publication in ***Science***

# Charged-Particle Probing of X-Ray-Driven Inertial-Fusion Implosions

C. K. Li<sup>1\*</sup>, F. H. Séguin<sup>1</sup>, J. A. Frenje<sup>1</sup>, M. Rosenberg<sup>1</sup>, R. D. Petrasso<sup>1</sup>, P. A. Amendt<sup>2</sup>, J. A. Koch<sup>2</sup>, O. L. Landen<sup>2</sup>, H. S. Park<sup>2</sup>, H. F. Robey<sup>2</sup>, R. P. J. Town<sup>2</sup>, A. Casner<sup>3</sup>, F. Philippe<sup>3</sup>, R. Betti<sup>4</sup>, J. P. Knauer<sup>4</sup>, D. D. Meyerhofer<sup>4</sup>, C. A. Back<sup>5</sup>, J. D. Kilkenny<sup>5</sup> and A. Nikroo<sup>5</sup>

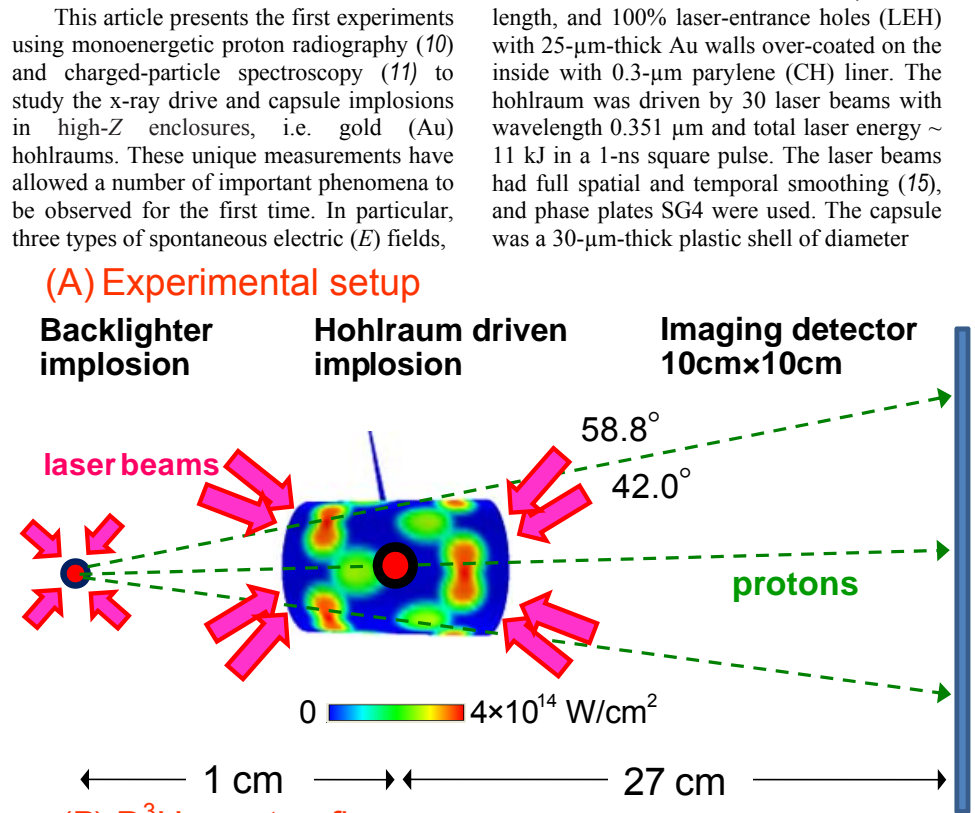
The first measurements of x-ray driven implosions with charged particles have resulted in unique and quantitative characterization of critical aspects of indirect-drive inertial fusion. Three types of spontaneous electric fields differing in strength by two orders of magnitude, the largest being nearly one-tenth of the Bohr field, were discovered with time-gated proton radiographic imaging and spectrally-resolved proton self-emission. The unparalleled views of the spatial structure and temporal evolution of both the laser drive in a hohlraum and implosion properties provide essential insight into, and modeling validation of, x-ray driven implosions.

differing by two orders of magnitude in strength with the largest approaching the Bohr field ( $= ea_0^{-2} \sim 5 \times 10^{11} \text{ V m}^{-1}$ , where  $a_0$  is the Bohr radius), were discovered. The experiments also demonstrate the absence of the stochastic filamentary pattern and striations generally found in laser-driven implosions (6). Other new results include the observations of plasma flow, supersonic jet formation, and self-generated magnetic ( $B$ ) fields (12,13); the determinations of areal density ( $\rho R$ ) and implosion symmetry; and the sampling of different implosion phases.

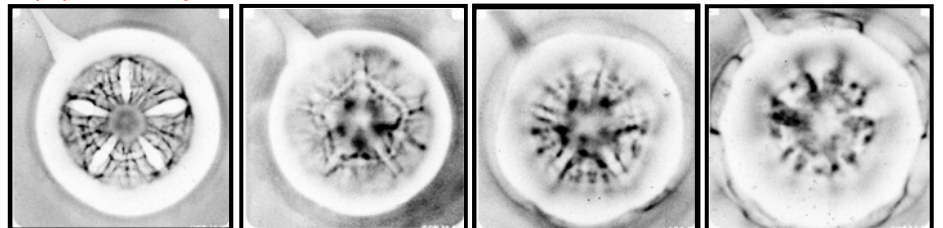
The experiments were performed at the OMEGA laser facility (14). The backlighting experiment is shown schematically in Fig. 1A. The hohlraum had a 2.4-mm diameter, 3.8-mm length, and 100% laser-entrance holes (LEH) with 25- $\mu\text{m}$ -thick Au walls over-coated on the inside with 0.3- $\mu\text{m}$  parylene (CH) liner. The hohlraum was driven by 30 laser beams with wavelength 0.351  $\mu\text{m}$  and total laser energy  $\sim 11 \text{ kJ}$  in a 1-ns square pulse. The laser beams had full spatial and temporal smoothing (15), and phase plates SG4 were used. The capsule was a 30- $\mu\text{m}$ -thick plastic shell of diameter

Understanding and characterizing x-ray drive and capsule implosions is critical to indirect-drive inertial confinement fusion (ICF) (1-3), a primary approach to achieving nuclear fusion ignition at the newly commissioned National Ignition Facility (NIF). Properties of the x-ray drive are also of fundamental scientific importance for a wide range of basic and applied high-energy-density physics (HEDP), including laboratory astrophysics, space physics, and materials sciences (4,5). Conventionally, diagnosing drive and implosions in these experiments has relied on techniques utilizing x rays, ultraviolet or visible light, and fusion neutrons. Although they have inherent sensitivity to both plasma density and field structures (6-9), charged particles have not previously been used because of practical limitations and challenging complexities, which have recently been overcome.

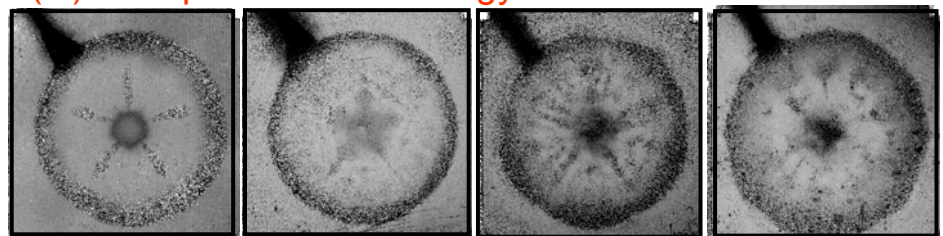
Fig 1. (A) Schematic of the experimental setup, with proton backlighter, hohlraum-driven implosion, CR-39 imaging detector, and laser drive beams. Fifteen laser beams entered each end of the hohlraum: 5 with incident angle 42° and 10 with angle 58.8°. The colors shown on the hohlraum wall indicate the laser intensity distribution [modeled by VISRAD (26)]. The proton backlighter was driven by 30 laser beams with total laser energy  $\sim 11 \text{ kJ}$  in a 1-ns square pulse. The 15-MeV  $\text{D}^3\text{He}$  backlighting protons (16) passed through the laser-driven hohlraum, sampling plasma conditions and capsule implosions at different times. Images in (B) show proton fluence (within each image, darker means higher fluence), while images in (C) show proton mean energy (within each image, darker means more proton energy loss and therefore more matter traversed). The gray-scale mapping for image display is different in each image. The capsule-mounting stalk appears in the upper left corner of each image.



(B)  $\text{D}^3\text{He}$  proton fluence



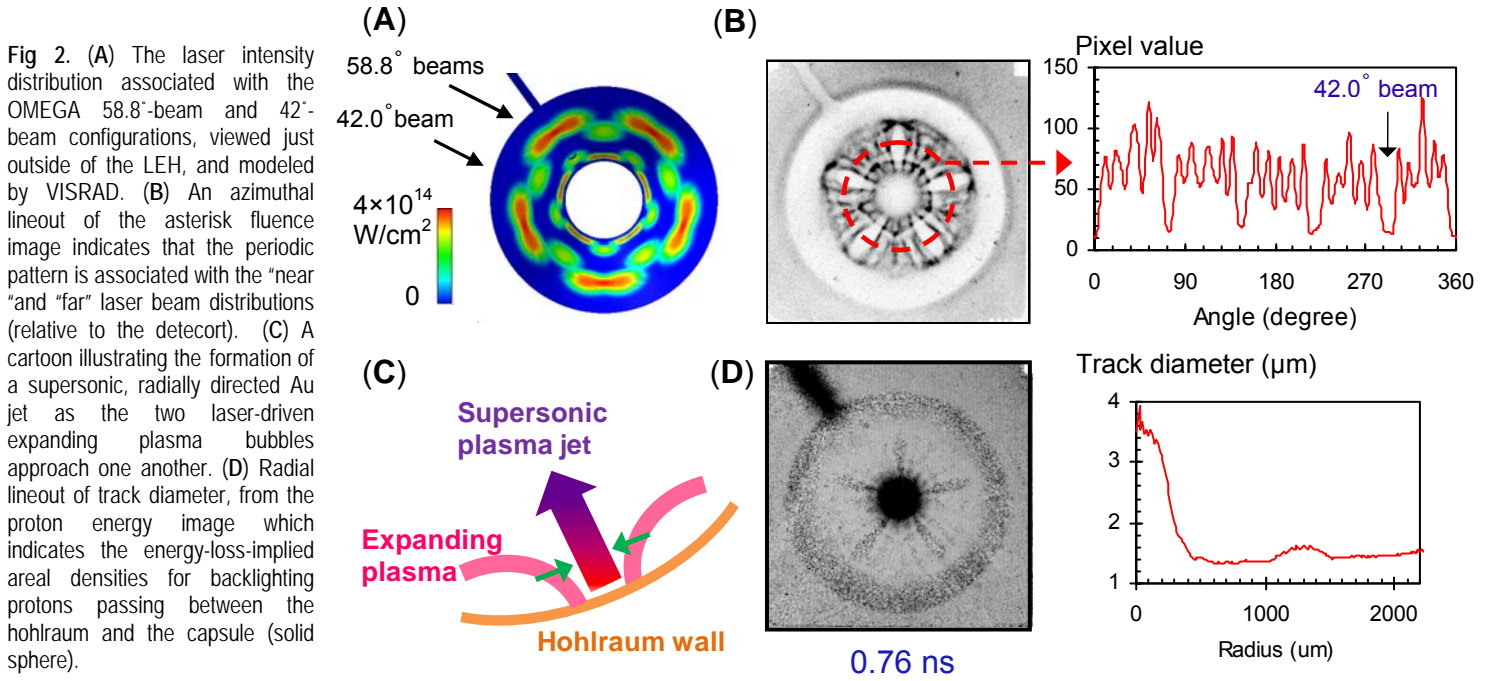
(C)  $\text{D}^3\text{He}$  proton mean energy



0.85 ns      1.60 ns      2.17 ns      2.79 ns

<sup>1</sup>Plasma Science and Fusion Center, Massachusetts Institute of Technology, Cambridge, MA 02139, USA. <sup>2</sup>Lawrence Livermore National Laboratory, Livermore, CA 94550, USA. <sup>3</sup>CEA/DIF, Arpajon Cedex, France. <sup>4</sup>Laboratory for Laser Energetics, University of Rochester, Rochester, NY 14623, USA. <sup>5</sup>General Atomics, San Diego, CA 92186, USA

\* Email: ckli@mit.edu



550 μm filled with 50 atm H<sub>2</sub> or D<sub>2</sub> gas. The designed radiation temperatures ( $\sim 150$  eV) and consequent capsule compression ( $\approx 10$ ) were modestly low. The backlighter was a D<sup>3</sup>He-gas-filled, glass-shell capsule with a 420-μm diameter and a 2-μm shell thickness, imploded by 30 laser beams. Two types of fusion protons with discrete birth energies of 14.7 and 3.0 MeV are produced in nuclear fusion reactions (D+<sup>3</sup>He $\rightarrow$ α+p and D+D $\rightarrow$ T+p)  $\sim 80$  ps. The images were recorded by CR-39 track detectors and the timing of the proton sampling was adjustable (6-10).

Radiographs made by 15-MeV D<sup>3</sup>He protons (16) covering a typical ICF implosion sequence are shown in Fig. 1. The image contains both spatial and energy information because the CR-39 detector records the position and energy of each individual proton (6-10). The images are displayed to show either proton fluence versus position (Fig. 1B) or proton mean energy versus position (Fig. 1C), to provide time-dependent information about field distributions, capsule compression, and hohlraum plasma conditions.

A striking feature shown in both fluence (Fig. 1B) and energy images (Fig. 1C) is a five-pronged asterisk-like pattern surrounding the imploding capsule. To explore this structure, a solid CH sphere driven with identical conditions was imploded, as shown in Fig. 2. With this solid sphere there is no shock wave breakout and no acceleration implosion phase (3), in contrast to the example in Fig. 1. The plasma conditions and five-pronged asterisk-like structure inside the hohlraums remain nearly identical for the two target types. Figure 2A shows the simulation of the laser intensity distribution associated with the OMEGA 58.8°- and 42.0°-beam configurations, viewed from a location just outside the LEH. The ten 58.8° laser beams

are grouped to form five pairs. An azimuthal lineout of the fluence image (Fig. 2B) indicates that the asterisk spokes are formed between two expanding plasma bubbles that are generated by “nearest neighbor” (58.8°) laser beam pairs (illustrated in Fig. 2A), while the periodic patterns (narrow fingers) between these spokes are associated with the remaining laser beam distributions.

A physical picture of the formation of the asterisk spokes is described as follows. For the experimental conditions, the expanding plasma bubbles [electron temperature  $T_e \sim 1$  keV, ion temperature  $T_i \sim 10$  eV, and electron density  $n_e$  (in units of critical electron density at 0.35 μm)  $\sim 0.1n_c$ ] (9) generated on the hohlraum wall near the laser spots are governed by plasma fluid dynamics (the ratio of thermal pressure to  $B$  field pressure,  $\beta \equiv 8\pi n_e k T_e B^{-2} \gg 1$ ). Their hydrodynamic expansion is scaled by the sound speeds [ $C_s \sim (ZT_e m_i^{-1})^{1/2} \sim 250 \mu\text{m ns}^{-1}$  for CH and  $\sim 150 \mu\text{m ns}^{-1}$  for Au, where  $Z$  is the average ion charge state]. For an adiabatic rarefaction expansion of an ideal gas, the expansion speed is  $3C_s$ , close to the observed jet speed ( $\sim 4C_s$ ). Furthermore the hot electrons advancing

ahead of the rarefaction expansion due to their high mobility may further boost the motion of leading edge CH and Au ions ablating off the hohlraum wall by an additional sound speed ( $\sim C_s$ ) factor (9). With  $\sim 200 \mu\text{m}$  between pairs of bubbles (Fig. 2A), it is observed that adjacent CH bubbles coalesce in  $\sim 0.1$  ns and reach the hohlraum axis in  $\sim 1$  ns, with the Au plasma bubble trailing behind (Fig. 2C).

To identify potential mechanisms for generating the spoke-like structure, we consider whether the image features seen in the region between the capsule and the hohlraum wall are due to scattering in the plasma or to proton deflections by  $E$  or  $B$  fields. This analysis is helped by the fact that nearly simultaneous images are recorded with two different but very accurately-known proton energies. For scattering in matter, deflection angles vary inversely with the proton energy ( $\theta \propto \varepsilon_p^{-1}$ ) (17). For  $B$  fields, it follows from the Lorentz force law that the deflection angles are inversely proportional to the square root of the proton energy ( $\theta \propto \varepsilon_p^{-1/2}$ ) (17), while those due to  $E$  are inversely proportional to the proton energy ( $\theta \propto \varepsilon_p^{-1}$ ) (17). The energy scaling due to  $B$  is unique,

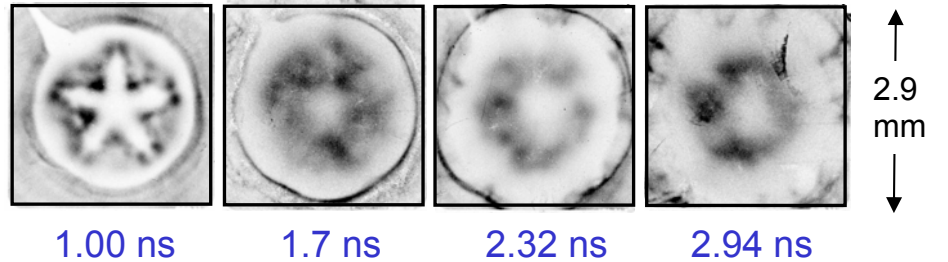


Fig. 3. 3.3-MeV DD proton radiographs of the same series of implosions shown in Fig. 1B (within each image, darker means higher fluence). The slightly different times are due to the slower proton velocities and longer flight times. The smeared spatial structures are caused by the fields and scattering. The variations of these images indicate temporal evolution of the fields, plasma flow, and implosions.



while that due to  $E$  and scattering is degenerate. Deflections due to scattering are accompanied by an energy loss, while those due to transverse  $E$  fields are not. Thus, discrimination between the two effects is possible.

The  $B$  field can be excluded by symmetry. The five-pronged asterisk-like pattern shown in Fig. 1 and 2 provides a constraint that rules out the possibility of self-generated  $B$  fields as a major cause for the formation of this structure, since the toroidal  $B$ -field topology around the laser spots or radial jets cannot result in azimuthal proton deflections.

With the  $B$  field excluded, the other two possible mechanisms for deflecting the proton trajectories are intense, local  $E$  fields associated with strong azimuthally-oriented electron pressure gradients ( $\nabla p_e$ ) in the spokes, and proton scattering in the spokes.

The possibility that the proton deflection is mostly caused by scattering that deflects protons out of the dense spoke can be ruled out through the measurements of the proton energy loss. It can be shown (Fig. 1C,  $t = 0.85$  ns) that there is little energy loss for protons passing through the major spokes. In the regions between the five spokes (Fig. 1C and 2D), there are high-contrast features in the fluence image, including the counterparts of the spokes generated by the “far” beams on the other side of the hohlraum, but very little variation in energy (Fig. 1C) (18)

This leaves the electric fields as the remaining cause. Using the spoke widths estimated in the images, the spreading of 15-MeV proton  $\delta_{15} \sim 90 \mu\text{m}$  (18),  $\int \mathbf{E} \times d\mathbf{l} \sim 3 \times 10^5$  V (where  $d\mathbf{l}$  is the differential path length along the proton trajectory through the field area). Taking a scale length  $\sim 1$  mm (the size of laser spot) for field in a jet-spoke results in  $E \sim 3 \times 10^8$  V  $\text{m}^{-1}$  with field directions pointed away from the spoke. This is the first time such strong, local  $E$  fields inside the hohlraum have been inferred even though the cavity is effectively a Faraday cage (9). The effects of such fields can impact important physics issues, including laser-plasma instabilities, modification of the plasma electron distribution, and implosion symmetry.

Whereas the structures of spokes and fingers inside the hohlraums were largely the result of the 15-MeV proton deflection by internal  $E$  fields (Fig. 1 and 2), the apparent increasing hohlraum size with time, as indicated in Fig. 3, is attributed to the 3-MeV protons scattered off the plasmas from the CH liner flowing out of the hohlraum ends, since the positive potential on the hohlraum wall has largely decayed even before the end of the laser pulses, as indicated by the laser-irradiated unlined hohlraums (9).

Another feature in Fig. 1B of note is that a fluence peak occurs in the capsule center during the early stages of the implosion ( $t = 0.85$  ns), but a fluence dip occurs at later times ( $t = 1.6 - 2.17$  ns). This observation is quantified in the radial lineouts shown in Fig.

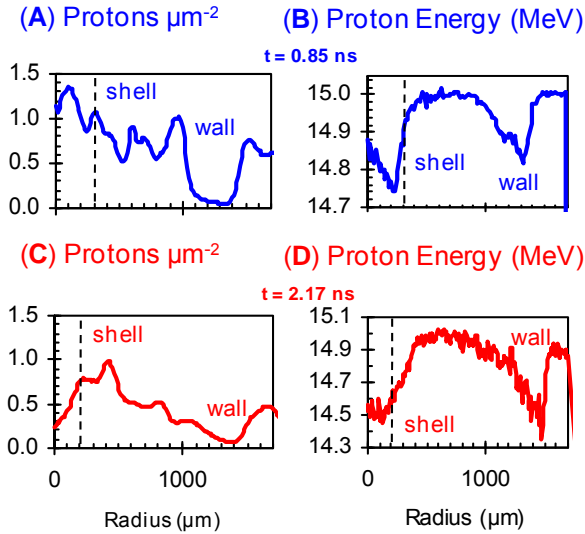


Fig. 4 Radial profiles of proton fluence images and energy images at  $t = 0.85$  ns [blue color, (A) and (B)], and at 2.17 ns [red color, (C) and (D)] from Figs. 1B and 1C, respectively. The profiles are averaged over azimuthal angle, excluding the stalk region. The difference in fluence levels outside the two capsules is due to the difference in the backlighter proton yields.

4A and 4C. While it has been observed in directly-driven spherical implosions (7), this is the first time such a phenomenon has been measured in x-ray driven implosions. In these and the earlier experiments the deflection of proton trajectories is attributed to self-generated radial  $E$  fields with strength  $10^9$ - $10^{10}$  V  $\text{m}^{-1}$  that are initially directed inward and eventually reverse direction (7,19). Furthermore, the effects of proton scattering in the shell (which sends some of the protons toward the image center and some away) play a minor role. A number of possible sources of such an  $E$  field, such as the gradient of plasma electron pressure, acceleration-induced charge separation, and shock-driven plasma polarization have been proposed to explain the field strength, unique spatial structure, and time evolution (7,19). This discovery will have important implications for ICF implosions; as an example, recent work has demonstrated that such a field leads to a fusion yield anomaly (20) through enhanced barodiffusion of different fuel species.

A common feature of the direct-drive implosions is the presence of striations around the capsule or solid CH sphere (6). No stochastic filamentary pattern was observed in the fluence images for x-ray driven implosions, however (Fig. 1 and 2). This result is important for understanding the role fields in laser and x-ray absorption, instabilities, and thermal transport involved in laser-plasma interactions.

To further characterize the capsule implosion history, quantitative information at different times is extracted from the radial lineouts through the centers of each of the individual images in Fig. 1C. The radial profiles of the mean proton energy (Fig. 4B and 4D), [a function of the spatially resolved proton energy loss (7,21)] are used to infer the capsule  $\rho R$ , as shown in Fig 4B, for  $t = 0.85$  ns ( $\sim 2.5$  mg  $\text{cm}^{-2}$ ) and Fig 4D,  $t = 2.17$  ns ( $\sim 8$  mg  $\text{cm}^{-2}$ ), indicating more energy loss at later time due to greater compressions.

To complement the backlighting approach

and give further insight into x-ray drive and implosion dynamics, another method -- high-resolution spectrometry of self-emitted charged particles from imploded capsules (11) -- has been used. Several important physical quantities, such as  $\rho R$  at nuclear burn time, fusion yields, and fields around the LEH axis, can be accurately measured through proton self emission (22). As shown in Fig. 5, 14.7-MeV  $\text{D}^3\text{He}$  protons generated during the implosion escape the shell, and provide information for characterizing implosion performance: first, the charged-particle yield -- a fundamental experimental complement to traditional neutron yields; second, measured proton energy loss which gives information about target areal density [ $\rho R = \int \rho(dE/dx)^{-1} dE$ ] (21); and third, measurements of  $\rho R$  at different angles to quantify implosion asymmetries (2,3). These measurements can be used to infer a number of important time-dependent implosion phenomena and parameters, such as fuel-shell mix (2,3), ion and electron temperatures, convergence ratio [ $C_r = Q(\rho R/\rho R_0)^{1/2}$ , where  $Q$  is a function of mass ablation], and spatially-resolved capsule structure (2,3).

In these experiments, the cylindrical vacuum Au hohlraum was 2.45 mm long with a 1.6 mm diameter and 50% LEH. The 647- $\mu\text{m}$  diameter CH capsule had a shell thickness of 48.2  $\mu\text{m}$  and was filled with 50 atm of  $\text{D}^3\text{He}$  (at equal number densities) gas. The hohlraum was driven by 40 beams with total laser energy of 19.7 kJ in a 1-ns square pulse.

Figure 5 shows data collected from  $\text{D}^3\text{He}$  protons produced during the nuclear burn: self-emission, spectrally resolved one-dimensional images and energy spectra. The narrow high-energy peak in each spectrum is associated with shock-flash burn (23), and the broad low-energy peak with compression burn. After correcting the proton spectrum seen at the equator for the measured energy loss through the 30- $\mu\text{m}$  hohlraum wall, the two peaks are found to have the same energies as those seen through the LEH. Values of  $\rho R$

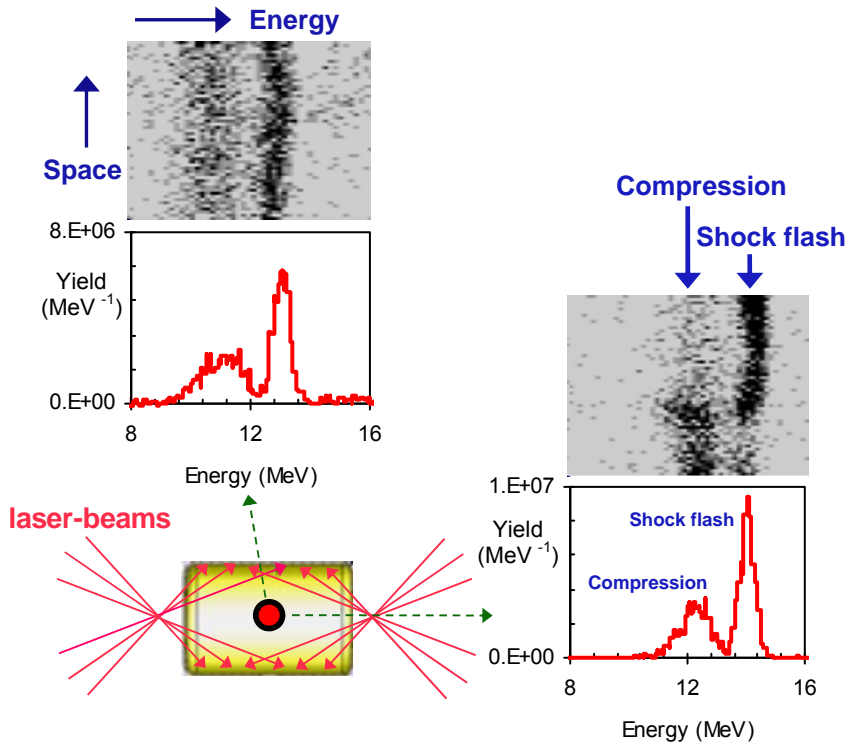


**Fig.5** The spectra and images of self-emitted protons generated from the fusion reaction of D and  $^3\text{He}$  in an x-ray driven ICF implosion (OMEGA shot 54744), measured simultaneously at two different directions. The proton yields associated with shock-coalescence burn [the narrow high-energy peak (bang, in image)] and compression burn [the broad low-energy peak (bang)] are clearly measured by the energy spectra and spectrally-selected images. It is shown that in the direction along LEH, the spatial structure of proton flux is nonuniform (compared with the image along the equator) at both shock flash and compression burn times, with opposing distribution.

inferred from the measured proton energy losses due to passage through the capsule shell indicate that  $\sim 20 \text{ mg cm}^{-2}$  is achieved at shock flash time and  $\sim 80 \text{ mg cm}^{-2}$  at the compression burn time in both the polar (toward LEH) and the equatorial directions. These are the first reported measurements using charged particles in x-ray-driven implosion; the technique will provide a new and powerful diagnostic for future experiments.

While the proton fluence in the direction of the equator is spatially uniform, the fluence in the LEH direction shows nonuniformities that are different for the two energy components (Fig. 5). Since they are generated at different times (separated by about  $\sim 200 \text{ ps}$  between the shock flash and compression burn), the nonuniformities have significantly evolved over this time interval. This distribution is not likely to have been caused by proton scattering off the plasmas, because the measured proton energies along both LEH and the equator are very similar. This suggests that the proton fluence nonuniformity is due to self-generated  $B$  or  $E$  fields near the LEH that do not cause proton energy loss but deflect their trajectories. Since shock-flash protons

selected by detector have probed a different line-of-sight than the different compression-generated protons, they might see different static small-scale fields. The strength of this  $B$  field is estimated to be  $\sim 2.5 \times 10^5 \text{ Tesla-}\mu\text{m}$ . The scale length (the radius of the laser spot) is about  $500 \mu\text{m}$ , suggesting that the  $B$  field is about  $500 \text{ Tesla}$  ( $5 \text{ megaGauss}$ ). If the nonuniformities are due to the  $E$  field, the strength required  $\sim 5 \times 10^{10} \text{ V m}^{-1}$ , is about one-tenth of the Bohr field, a fundamental field strength for stripping bound electrons. This value is about 10 times the strength estimated from Faraday's law ( $\partial B/\partial t = -\nabla \times E$ ) based on the above-estimated  $B$  field strength and  $200 \text{ ps}$  time scale, suggesting that the time scale for field variation should be  $\sim 10$  times faster. The high fields are likely generated in the region near the LEH where the outward-directed axial plasma becomes increasingly resistive after the laser drive ends, leading to the generation, growth and saturation of low-mode number magneto-instabilities (24). The data suggest that the spatial structure or the directions of such fields undergoes rapid changes between the time of shock flash and compression burn.

## References and Notes

1. J. Nuckolls *et al.*, *Nature* **239**, 139 (1972).
2. J. Lindl, *Inertial Confinement Fusion* (Springer-Verlag, New York, 1999).
3. S. Atzeni, J. Meyer-Ter-Vehn, *The Physics of Inertial Fusion* (Clarendon, Oxford 2004).
4. B. A. Remington *et al.*, *Science* **284**, 1488 (1999).
5. R. P. Drake, *High-Energy-Density Physics* (Springer Press, New York, 2006)
6. J. R. Rygg *et al.*, *Science* **319**, 1223 (2008).
7. C. K. Li *et al.*, *Phys. Rev. Lett.* **100**, 225001 (2008).
8. R. D. Petrasso *et al.*, *Phys. Rev. Lett.* **103**, 085001 (2009).
9. C. K. Li *et al.*, *Phys. Rev. Lett.* **102**, 205001 (2009).
10. C. K. Li *et al.*, *Phys. Rev. Lett.* **97**, 135003 (2006).
11. F. H. Séguin *et al.*, *Rev. Sci. Instrum.* **74**, 975 (2003).
12. S. I. Braginskii, *Review of Plasma Physics 1* (Consultants Bureau, New York, 1965).
13. M. G. Haines, *Phys. Rev. Lett.* **78**, 254 (1997).
14. J. M. Soures *et al.*, *Phys. Plasmas* **3**, 2108 (1996).
15. D. D. Meyerhofer *et al.*, *Phys. Plasmas* **8**, 2251 (2001).
16. A slight upshift from its birth energy is caused by positive charging of the backlighter target.
17. J. D. Jackson, *Classical Electrodynamics* (Wiley, New York 1975).
18. The measured width (FWHM) in Fig. 1B is  $\Delta_{15} \sim 260 \mu\text{m}$  ( $t = 0.85 \text{ ns}$ ), which includes both the width  $W$  of the jet itself and the spreading  $\delta_{15}$  of the 15-MeV protons:  $\Delta_{15}^2 = W^2 + \delta_{15}^2$ . The corresponding 3-MeV image ( $t = 1.00 \text{ ns}$  in Fig. 3.) represents a slightly later time due to the slower velocities of the lower-energy protons,  $\Delta_3 \approx 2 \Delta_{15}$ . Since  $\delta_3 = (15/3) \delta_{15} = 5 \delta_{15}$ , and  $\Delta_3^2 = W^2 + \delta_3^2$ , it follows that  $\delta_{15} \approx 90 \mu\text{m}$ . Taking the plasma scale length (laser spot size on the wall)  $L \sim 1.2 \text{ mm}$ , the scattering angle in radians can be estimated  $\langle \theta \rangle \sim 0.5 \delta_{15}/L \approx 0.037$ . This amount of spreading can be shown to require about  $\rho L \approx \rho L_{\text{rad}} (pv/15 \text{ MeV})^2 < \theta^2 \sim 33 \text{ mg cm}^{-2}$  of Au, where  $pv = 30 \text{ MeV}$  and  $\rho L_{\text{rad}} \sim 6 \times 10^3 \text{ mg cm}^{-2}$  for Au (25). If the 5-spoke structure in the images is caused primarily by proton scattering in the spokes, this amount of  $\rho L$  would lead to  $\sim 1\text{-MeV}$  energy loss for 15-MeV protons, which is substantially more than observed in Fig. 1C [energy loss consistent with scattering if assume CH in bubble would be even greater ( $\approx 15 \text{ MeV}$ )].
19. P. A. Amendt *et al.*, *Plas. Phys. Contr. Fus.* **51**, 124048 (2009).
20. J. R. Rygg *et al.*, *Phys. Plasmas* **13**, 052702 (2006).
21. C. K. Li, R. D. Petrasso., *Phys. Rev. Lett.* **70**, 3059 (1993).
22. Since the backlighting proton fluence is reduced or even blocked along the hohlraum axis due to the deflection and/or scattering in the compressed capsule core (Fig. 1-4).
23. R. D. Petrasso *et al.*, *Phys. Rev. Lett.* **90**, 095002 (2003).
24. C. K. Li *et al.*, *Phys. Rev. E.* **80**, 016407 (2009).
25. T. A. Lasinski *et al.*, *Rev. Mod. Phys.* **45**, s1 (1973).
26. J. J. MacFarlane, *J. Quant. Spectr. Rad. Transfer*, **81**, 287 (2003).
27. This work was supported in part by US DOE and LLE National Laser User's Facility (DE-FG52-07NA28059 and DE-FG03-03SF22691), LLNL (B543881 and LDRD-ER-898988), CEA/DIF (France, Cooperative agreement No. DE-FC52-08NA28302), LLE (414090-G), FSC at Uni. Rochester (412761-G), and General Atomics (DE-AC52-06NA27279).